CFD Simulations of Bubbling/Collapsing Fluidized Beds for Three Geldart Groups

Susan J. Gelderbloom
Dow Corning Corp., Midland, MI 48686

Dimitri Gidaspow
Illinois Institute of Technology, Dept. of Chemical and Environmental Engineering, Chicago, IL 60616

Robert W. Lyczkowski
Argonne National Laboratory Energy Systems Div., Argonne, IL 60439

A multiphase computational fluid dynamics (CFD) model was applied to a commonly used industrial experiment known as the collapsing fluidized-bed experiment. The experiment involves several hydrodynamic regimes including the bed expansion, bubbling, sedimentation, and consolidation of the fluidized bed. The CFD model is capable of predicting all four of these regimes. The three Geldart Groups, C, A, and B were simulated in a bubbling and subsequently collapsing fluidized bed. Results show that hydrodynamic Models A and B, the use of the modified Ergun equation or the MFIX code drag models, and solids rheology have limited impact on the bubbling- and collapsing-bed simulations. The major finding of this study is that the solids modulus, G, is the controlling parameter during the consolidation regime. The simulated bubble sizes and bed collapse rates for all three Geldart groups were found to be within reported experimental error. The computed high turbulent intensity of Geldart Group A particles also agrees with data in the literature measured using an acoustic shot noise probe. It is also demonstrated that the traditional interpretation of the collapsing bed as consisting of separate bubble escape and sedimentation regimes is incorrect and that, in fact, they occur simultaneously.

Introdution

The collapsing fluidized-bed experiment, first described by Rietema (1967), has been used to understand the dense-phase regime of fluidization, and is still commonly used today (Geldart et al., 1984; Geldart and Wong, 1984; Grace, 1992; Barreto et al., 1988; Tianxiong et al., 1982; Yang et al., 1997; Formisani et al., 2002, for example). This experiment consists of fluidizing a bed to the quasi-steady-state condition and then suddenly stopping the gas flow. Observations of the bed are made as the gas escapes and the particulate phase settles and consolidates. This technique gives general properties of the dense-phase regime, including the average void fraction and superficial gas velocity (Weimer and Quarderer, 1984). This technique has also been used to gain insight as to the effects of other variables such as high pressure and/or high temperature (Weimer and Quarderer, 1984; Lettieri, 1999). Application of this technique is not limited to predicting the behavior of fluidized beds, but is also valuable in the understanding and design of the standpipes and hoppers.

This investigation originated from an industry need to better understand the current computational fluid dynamics (CFD) hydrodynamics of fluidization capabilities. The collapsing fluidized-bed experiment is a small, well-defined experiment that involves many different hydrodynamic phenomena. The bed expansion, bubbling, sedimentation, and consolidation all play important roles in the collapsing fluidized-bed experiment. The capability of CFD to correctly model this experiment would increase the confidence of industrial users. The modeling of the collapsing fluidized-bed experiment can also serve to verify key particle characteristics and refine the hydrodynamic model before attempting to simulate more complex reacting systems. The following section gives an overview of the experiment.

Correspondence concerning this article should be addressed to R. W. Lyczkowski.

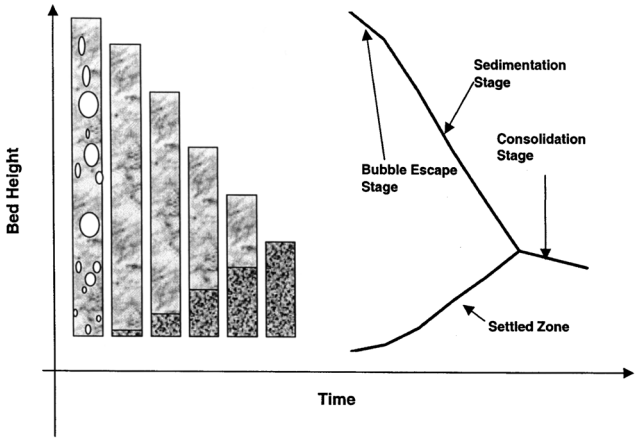

Figure 1. Stages of the collapsing fluidized-bed experiment (classic description).

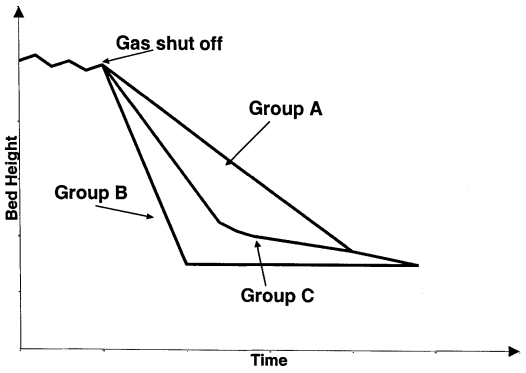

Figure 2. Idealized collapsing fluidized-bed curves for Geldart Groups C, A, and B.

Collapsing Fluidized-Bed Experiment

In the classic description of the collapsing fluidized-bed experiment (Rietema, 1967), three separate stages are identified, as shown in Figure 1. In the first stage, called the bubble escape stage, the bubbles in the bed rise to the top and escape. In the second stage, called the sedimentation stage, the bed height falls. During this stage the gas-phase volume fraction, also referred to as the void fraction, at the bottom of the bed decreases, creating a settled zone, while the void fraction in the rest of the bed remains relatively constant. The interface between the settled zone and the rest of the bed continues to rise and the overall bed height continues to fall. The rate of the settled zone interface rise is slower than the bed-height collapse. A one-dimensional (1-D) mass balance shows that the settled zone increases at a slower rate than the fluidized dense zone decreases (Rietema, 1991). The third stage, called the consolidation stage, begins when the top of the bed reaches the interface of the settled zone. During this third stage there is a slow compaction, depending on the particulate characteristics.

Geldart Groups and the Collapsing Fluidized-Bed Experiment

The collapsing fluidized-bed experiment illustrates the different behavior of the Geldart Groups (Geldart et al., 1984; Geldart and Wong, 1984; Tung and Kwauk, 1982; Grace, 1992). When Geldart Group B particles are fluidized, large bubbles are produced. When the fluidized bed containing Geldart Group B particles is collapsed, the bubbles leave rapidly and the bed height decreases very quickly. Barreto et al. (1988) and Yang et al. (1997) observed that this happens so quickly that little useful data can be obtained. There is very little published data quantifying the rate of collapse of Geldart Group B particles.

With Geldart Group A particles, the bubbling bed height collapses quickly as the bubbles escape from the top of the bed and sedimentation occurs, with the bed freeboard falling at a constant rate until the consolidation stage is reached. This rate of bed collapse, or the rate of the freeboard fall, is often interpreted as the superficial gas velocity of the dense-phase regime (Geldart et al., 1984; Weimer and Quarderer, 1984).

The rate of bed collapse, or rate of freeboard fall, for Geldart Group C particles, which are considered to be cohesive, has a more exponential shape to the curve, with a quick initial decrease followed by a slower decline. The initial quick drop of the bed height for cohesive particles is believed to be due to the fracture and channeling of the bed, allowing the quick escape of the gas (Geldart and Wong, 1984). The subsequent slower decline of the bed height is a result of the trapped gas exiting in the interstitial spaces of the particles and possibly the cohesion between the particles. Figure 2 represents an idealized summary of the preceding discussion.

Variability in Experimental Results

Grace (1992) has reviewed the lack of consistency in the experimental methodology of the collapsing fluidized-bed experiment. Most of the inconsistencies in the data can be explained by differences in the venting of the collapsing bed. With a single vent, the air in the wind box, coupled with a high-pressure drop through the distributor, can introduce a substantial volume of air into the bed during the collapse. This problem can be eliminated by double venting, both the wind box and the collapsing bed simultaneously. Grace also cautions against over venting the wind box, causing air to back feed from the bed into the wind box.

Four different sets of data (Geldart and Wong, 1984; Tung and Kwauk, 1982; Abrahamsen and Geldart, 1980; Lettieri, 1999) give similar results for collapse velocities, as analyzed by Gelderbloom (2001). Collapse velocity values range from 0.05 cm/s to 0.6 cm/s for these four data sets.

The confusion in the literature not only involves the experimental procedure as discussed by Grace (1992) and summarized earlier, but also in the identification of the collapse stages. Barreto et al. (1988) and Yang et al. (1997) report entire collapse-rate curve data instead of only collapse-velocity values. These curves show a much faster bed collapse, followed by a slow consolidation curve. This consolidation portion of the curve is consistent with Geldart et al.'s. (1984) collapse-velocity values. Without entire collapse-rate curves, collapse-velocity data are subject to misinterpretation.

Barreto et al.'s (1988) research also found that the bed-height collapse rate for zeolite 24 (particle diameter 53μm) is equal to the volumetric flow rate of the fluidizing gas into the

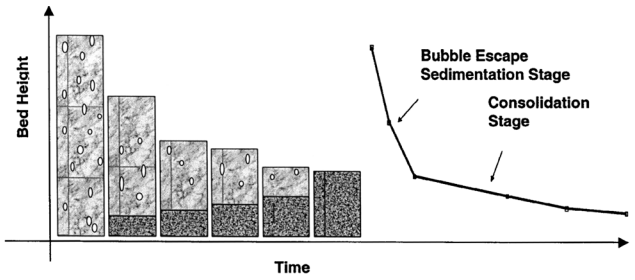

Figure 3. Stages of the collapsing fluidized-bed experiment (more accurate description).

bed, divided by the cross-sectional area of the bed (the inlet gas velocity). Barreto et al.'s (1988) data spans the range of 1 to 7 cm/s inlet gas velocity and pressures between 0.1 to 2.1 MPa (1 to 20 atm). Yang et al.'s (1997) bed-height curves show an initial collapse during the bubble escape stage, to be between 32 and 37 cm/s for particles of 19- to 59-μm diameter. These experiments were performed with an inlet gas velocity of 33 cm/s. These experimental data are also consistent with Barreto et al.'s (1988) proposal that the inlet gas velocity is approximately equal to the bed-height collapse velocity during the bubble escape stage.

It is concluded that the bed-collapse velocity data reported by Geldart et al. (1984), Tung and Kwauk (1982), Abrahamsen and Geldart (1980), and Lettieri (1999) are actually the consolidation collapse rates, as described in Figure 1. The bubble escape occurs simultaneously with the sedimentation. There is significant bed-height loss during this bubble escape/sedimentation period. A more accurate depiction of the collapsing-bed experiment is shown in Figure 3. This representation combines the bubble escape and sedimentation stages and corrects the scenario shown in Figure 1.

Computer Program

The code used in this research is a public domain computer program MFIX (Syamlal et al., 1993) developed by the National Energy Technology Laboratory (NETL) in Morgantown, WV, and is available on the Internet at http://www.mfix.org. This code was chosen because it is a well-documented source code that provided the ability to program any desired new model as well as having preprogrammed options, such as hydrodynamic Models A and B, different drag laws, various solids moduli, and various numerical solution schemes. The MFIX code also comes with a convenient postprocessor code that provides a single command animation of the results as well as quantitative data retrieval. MFIX is set up with a staggered grid arrangement, as shown in Figure 4. Scalar values are stored at the cell centers and velocity vector-component values are stored on the cell faces. The scalar quantities including pressure, void fraction, temperature, and mass fraction are all solved on the main grid. The velocity vector components are solved on a staggered grid. Thus, for a three-dimensional simulation, four grids are used for the solution.

Hydrodynamic Model

This section describes the hydrodynamic equations solved in the MFIX code (Syamlal et al., 1993).

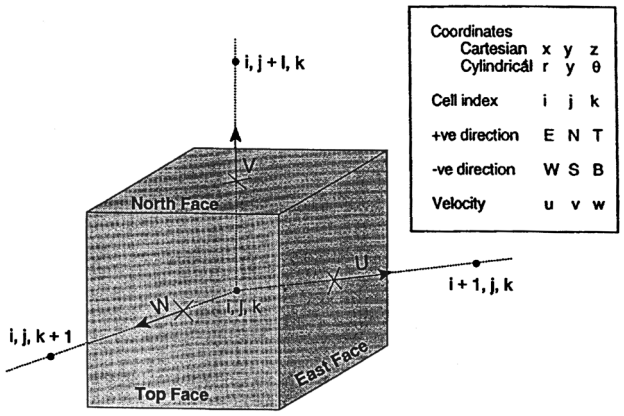

Figure 4. Nomenclature and computational domain for MFIX code.

Continuity equations

Fluid-phase continuity:

$$\frac{\partial}{\partial t}(\epsilon_g \rho_g) + \nabla\cdot(\epsilon_g \rho_g \boldsymbol{v}_g) = 0 \tag{1}$$

Solids-phase continuity

$$\frac{\partial}{\partial t}(\epsilon_s \rho_s) + \nabla\cdot(\epsilon_s \rho_s \boldsymbol{v}_s) = 0 \tag{2}$$

Momentum equations (hydrodynamic Model A)

Fluid-phase momentum balance

$$\frac{\partial}{\partial t}(\epsilon_g \rho_g \boldsymbol{v}_g) + \nabla\cdot(\epsilon_g \rho_g \boldsymbol{v}_g \boldsymbol{v}_g) = -\epsilon_g \nabla P_g + \nabla\cdot\bar{\bar{\tau}}_g + F_{gs}(\boldsymbol{v}_s - \boldsymbol{v}_g) + \epsilon_g \rho_g g \tag{3}$$

Solids-phase momentum balance ($s = sl$)

$$\frac{\partial}{\partial t}(\epsilon_s \rho_s \boldsymbol{v}_s) + \nabla\cdot(\epsilon_s \rho_s \boldsymbol{v}_s \boldsymbol{v}_s) = -\epsilon_s \nabla P_g + \nabla\cdot\bar{\bar{\tau}}_s - F_{sg}(\boldsymbol{v}_s - \boldsymbol{v}_g) - F_{slm}(\boldsymbol{v}_{sl} - \boldsymbol{v}_{sm}) + \epsilon_g \rho_g g \tag{4}$$

Symbols are defined in the Notation.

Constitutive Closure Models

To allow closure of the preceding equations, the following models are used in the MFIX code (Syamlal et al., 1993).

Fluid-phase stress tensor

The gas-phase viscous stress tensor is given by

$$\bar{\bar{\tau}}_g = 2\epsilon_g \mu_g \bar{\bar{D}}_g - \frac{2}{3}\epsilon_g \mu_g tr\left(\bar{\bar{D}}_g\right)\bar{\bar{I}} \tag{5}$$

where

$$\bar{\bar{D}}_g = \frac{1}{2}\left[\nabla \boldsymbol{v}_g + \left(\nabla \boldsymbol{v}_g\right)^T\right] \tag{6}$$

Solids-phase granular stress tensor

Johnson and Jackson (1987) proposed dividing the solids-phase granular stress tensor into two regimes, viscous, $\bar{\bar{\tau}}_s^{v}$, and plastic, $\bar{\bar{\tau}}_s^{p}$. The model is switched from one to the other based on the packed-bed gas volume fraction, ϵ_g^*. This accounts for the solids flow below minimum fluidization.

The solids phase stress tensor is defined as

$$\bar{\bar{\tau}}_s = \begin{cases} -P_s^p \bar{\bar{I}} + \bar{\bar{\tau}}_s^p & \epsilon_g \le \epsilon_g^* \\ -P_s^v \bar{\bar{I}} + \bar{\bar{\tau}}_s^v & \epsilon_g > \epsilon_g^* \end{cases} \tag{7}$$

Plastic regime

The solids pressure is given by

$$P_s^p = \epsilon_s P^* \tag{8}$$

where

$$P^* = 10^{25}(\epsilon_g - \epsilon_g^*)^{10} \tag{9}$$

The solids-phase granular stress tensor for the plastic regime is given by

$$\bar{\bar{\tau}}_s^p = 2\mu_s^p \bar{\bar{D}}_s \tag{10}$$

where

$$\bar{\bar{D}}_s = \frac{1}{2}\left[\nabla \boldsymbol{\nu}_s + (\nabla \boldsymbol{\nu}_s)^T\right] \tag{11}$$

The solids-phase viscosity for the plastic regime is given by

$$\mu_s^p = \frac{P^* \sin\Phi}{2\sqrt{I_{2D}}} \tag{12}$$

where Φ is the internal angle of friction. The second invariant of the strain rate tensor is given by

$$I_{2D} = \frac{1}{6}\left((D_{s11} - D_{s22})^2 + (D_{s22} - D_{s33})^2 + (D_{s33} - D_{s11})^2\right) + D_{s12}^2 + D_{s23}^2 + D_{s31}^2 \tag{13}$$

Viscous regime

The solids-phase pressure is given by

$$P_s^v = K_1 \epsilon_s^2 \Theta \tag{14}$$

This model for the solids pressure is questionable, since recent work by Gidaspow and Huilin (1998) have shown that the kinetic part of the solids pressure must also be included. A more correct solids pressure model given by Gidaspow (1994) is

$$P_s^v = \epsilon_s \Theta \cdot \epsilon_s \tag{15}$$

The solids-phase granular stress tensor for the viscous regime is given by

$$\bar{\bar{\tau}}_s^v = \lambda_s^v tr\left(\bar{\bar{D}}_s\right)\bar{\bar{I}} + 2\mu_s^v \bar{\bar{D}}_s \tag{16}$$

where λ_s^v, is the second coefficient of viscosity given by

$$\lambda_s^v = K_2 \epsilon_s \sqrt{\Theta} \tag{17}$$

and the solids-phase viscosity is given by

$$\mu_s^v = K_3 \epsilon_s \sqrt{\Theta} \tag{18}$$

The constants K_1, K_2, and K_3 are defined as

$$K_1 = 2(1+e_m)\rho_s g_{o_m} \tag{19}$$

$$K_2 = 4 d_p \rho_s (1+e_m)\epsilon_s g_{o_m}/\left(3\sqrt{\pi}\right) - \frac{2}{3}K_3 \tag{20}$$

and

$$K_3 = \frac{d_p \rho_s}{2}\left\{\frac{\sqrt{\pi}}{3(3-e_m)}\left[1 + 0.4(1+e_m)(3e_m - 1)\epsilon_s g_{o_m}\right] + \frac{8\epsilon_s g_{o_m}(1+e_m)}{5\sqrt{\pi}}\right\} \tag{21}$$

The radial distribution function at contact, g_{o_m}, is that derived by Lebowitz (1964)

$$g_{o_m} = \frac{1}{\epsilon_g} + \frac{3\left(\sum_{\lambda=1}^{M} \frac{\epsilon_{s\lambda}}{d_{p\lambda}}\right) d_p}{2\epsilon_g^2} \tag{22}$$

Granular Temperature Equation

The MFIX code uses an algebraic expression for granular temperature derived from the energy equation of Lun et al. (1984). This assumes that the granular temperature is dissipated locally and neglects the convection and diffusion contributions, leaving only the generation and dissipation terms (Syamlal, 1987). The granular temperature is given as

$$\Theta = \left\{\frac{-K_1\epsilon_s tr\left(\bar{\bar{D}}_s\right) + \sqrt{K_1^2 tr^2\left(\bar{\bar{D}}_s\right)\epsilon_s^2 + 4K_4\epsilon_s\left[K_2 tr^2\left(\bar{\bar{D}}_s\right) + 2K_3 tr\left(\bar{\bar{D}}_s^2\right)\right]}}{2\epsilon_s K_4}\right\}^2 \tag{23}$$

with constant K_4 as

$$K_4 = \frac{2\left(1 - e_m^2\right)\rho_s g_{o_m}}{d_p\sqrt{\pi}} \tag{24}$$

Drag Force

This section describes the drag forces between the fluid and solids phases and between the solids phases.

Fluid – solids drag function

The MFIX code treatment of the drag correlation is based on the terminal velocity of fluids and the settling of beds. These expressions take into account void fraction and particle Reynolds number. The following drag function was proposed by Syamlal and O'Brien (1987) (which we will subsequently refer to as the Syamlal–O'Brien drag function

$$F_{gs} = \frac{3\epsilon_s\epsilon_g\rho_g}{4V_{rm}^2 d_p}\left(0.63 + 4.8\sqrt{V_{rm}/Re_s}\right)^2 |\boldsymbol{\nu}_s - \boldsymbol{\nu}_g| \tag{25}$$

where the Reynolds number is defined as

$$Re_s = \frac{\rho_g d_p |\nu_g - \nu_s|}{\mu_g} \tag{26}$$

The terminal velocity correlation for the solids phase used in the MFIX code (Syamlal et al., 1993) is derived from a correlation developed by Garside and Al-Dibouni (1977) as

$$V_{rm} = 0.5\left(A - 0.06Re_s + \sqrt{(0.0036Re_s)^2 + 0.12Re_s(2B - A) + A^2}\right) \tag{27}$$

$$A = \epsilon_g^{4.14} \tag{28}$$

$$B = \begin{cases} Q\epsilon_g^{1.28} & \epsilon_g \le 0.85 \\ \epsilon_g^R & \epsilon_g > 0.85 \end{cases} \tag{29}$$

where Q and R are user-defined quantities with defaults of

$$Q = 0.8 \quad \text{Adjust to match } U_{mf} \tag{29a}$$

$$R = 2.653 \quad \text{Adjust for function continuity.} \tag{29b}$$

The values of Q and R can be determined with the use of a spreadsheet (Syamlal, 1999). Inputs include fluid and solids physical properties and experimental values of minimum fluidization velocity and void fraction at minimum fluidization. The limitation of this technique is that there are conditions that will not give a meaningful value for Q or R. The experimental data that were targeted in this work were one of these conditions. The default values were, therefore, used in simulations that used the Syamlal–O'Brien drag function.

Solids – solids drag function

The solids–solids drag function in the MFIX code (Syamlal et al., 1993) given by

$$F_{slm} = \frac{3(1 + e_{lm})\left(\frac{\pi}{2} + \frac{C_{flm}\pi^2}{8}\right)\epsilon_{sl}\rho_{sl}\epsilon_{sm}\rho_{sm}\left(d_{pl} + d_{pm}\right)^2 g_{o_{lm}}|\boldsymbol{\nu}_{sl} - \boldsymbol{\nu}_{sm}|}{2\pi\left(\rho_{sl}d_{pl}^3 + \rho_{sm}d_{pm}^3\right)}, \tag{30}$$

with the multiple particles radial distributions function

$$g_{o_{lm}} = \frac{1}{\epsilon_g} + \frac{3\left(\sum_{\lambda=1}^{m}\epsilon_{s\lambda}/d_{p\lambda}\right)d_{pl}d_{pm}}{\epsilon_g^2\left(d_{pl} + d_{pm}\right)} \tag{31}$$

to accommodate two different particle diameters and densities denoted by *dpl*, *dpm*, *Psl* and *Psm* respectively. For the simulations done here, only a single particle size was used. The solids–solids drag function, F_{slm}, is a function of parameters including the coefficient of restitution, e_{lm}, the coefficient of friction, C_{flm}, and the radial distribution function, $g_{o_{lm}}$. This form is based on a simplified version of the kinetic theory described by Syamlal and O'Brien (1987).

Solids Pressure and Solids Modulus

The solids pressure exerted by particulates consists of three parts: (1) a kinetic portion due to random particle oscillations, (2) a collisional portion, and (3) a cohesive portion. For 75-μm Geldart Group A FCC particles, Gidaspow and Huilin (1998) determined a complete equation of state relating the solids pressure to the granular temperature. The cohesive portion of the solids pressure was determined from experimental radial distribution functions of statistical mechanics. For a solids volume fraction of 25% the cohesive pressure accounts for approximately 25% of the total solids pressure measured with a special differential solids pressure transducer. For Geldart Group C particles this cohesive pressure contribution may be much larger than for Geldart Group A particles. In the solids-phase momentum balance, Eq. 4, we need the derivative of the solids pressure. This gradient is known as the solids modulus, G, and is given by

$$G = \frac{\partial P_s}{\partial \epsilon_s} \tag{32}$$

In order to apply our hydrodynamic model to Geldart Group C particles, we need to know the cohesive contribution to the solids modulus. The procedure for experimentally obtaining this contribution is described in chapter 12 of Gidaspow's book (1994) for sedimentation of particles in a liquid. This procedure was used to obtain the solids modulus for settling of 10-nm silica particles in air (Jung and Gidaspow, 2002). In view of the absence of such data for Geldart Group A particles, various formulations proposed in the

literature were used in this study given by

$$G = n10^{D}(\epsilon - \epsilon^*)^{n-1} \quad \text{(Syamlal et al., 1993)} \quad (33)$$

$$G = 10^{A\epsilon + B} \quad \text{(Gidaspow and Ettehadieh, 1983)} \quad (34)$$

and

$$G = G_o e^{-c(\epsilon - \epsilon^*)} \quad \text{(Bouillard et al., 1989)} \quad (35)$$

where $\epsilon = \epsilon_g$.

The parameters for these three formulations used in this study are given by $n = 10$, $D = 25$, and $\epsilon^* = 0.43$ (Syamlal et al., 1993); $A = -8.76$ and $B = 5.43$ (Gidaspow and Ettehadieh, 1983); and $G_o = 1{,}0$, $c = 600.0$, and $\epsilon^* = 0.37$ (Bouillard et al., 1989). Values of the parameters in Eqs. 33 through 35 for other formulations are given in Gelderbloom (2001).

Both the Syamlal et al. (1993) and the Bouillard et al. (1989) solids modulus formulations behave nearly as step functions just below ϵ^*, which is defined as the void fraction at or slightly aboue the packed-bed void fraction, and quickly become extremely large, simulating "brick like" behavior (Bouillard and Gidaspow, 1991). The Gidaspow and Ettehadieh (1983) formulation does not display this behavior and produces much lower values of the solids modulus.

Computed Bubbles for Geldart Groups C, A, and B

This section describes simulations of a bubbling fluidized bed for the three Geldart Group C (cohesive), A (aerated), and B (bubbling). These groups (Geldart, 1973) are mapped as a function of particle size and density difference and fall into distinct regions. Bubbling bed simulations were extensively reviewed by Gidaspow (1994), Enwald et al. (1996), Kuipers et al. (1998), and Jackson (2000).

The bubbling fluidized-bed simulations were performed in a thin rectangular "two dimensional" fluidized bed, twice as tall as it was wide. The inlet boundary condition is a uniform distribution of gas at a set velocity across the bottom of the domain. The outlet, which spans the width of the top of the domain, was modeled as a constant-pressure outlet. The bed was filled to half its height with solids at a void fraction equal to 0.6. The sides were modeled as walls with zero slip for both gas and solids phases.

Table 1. Simulation Parameters for Geldart Group C, A, and B Particles

Geldart Group	C	A	B
Particle diameter (μm)	20	71	200
Particle material	Sand	FCC	Sand
Particle density (g/cm^3)	2.10	1.42	2.10
Inlet (superficial) gas Velocity (cm/s)	0.5	3	35
Minimum fluidization Velocity (cm/s)	0.035	0.32	3.2
Domain width (cm)	7	7	15
Domain height (cm)	15	15	45
Number of cells	90×195	90×195	90×280
Grid size (cm)	0.078×0.077	0.078×0.077	0.156×0.16
Coefficient of restitution	0.8	0.8	0.8
Drag parameters, Q and R	0.8–2.653	0.8–2.653	0.8–2.653
Internal angle of friction	30°	30°	30°
Shape factor	1.0	1.0	1.0

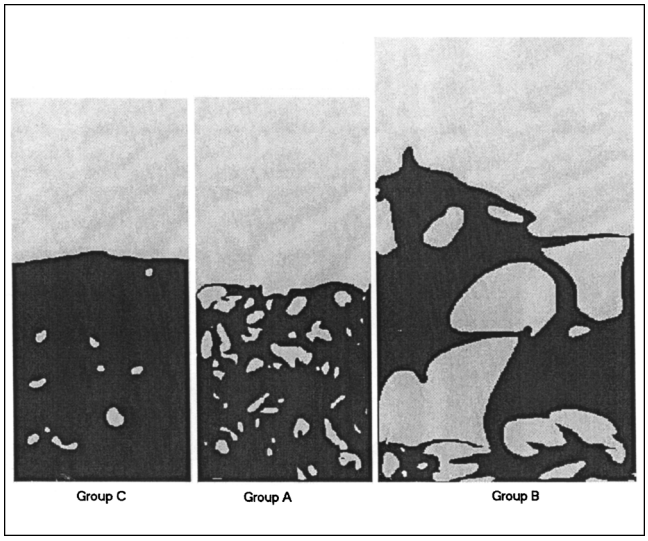

Figure 5. Comparison of computed bubbles for Geldart Groups C, A, and B.

Initial conditions set the y-direction gas velocities equal to the inlet fluidizing gas velocity divided by void fraction to yield the interstitial gas velocities. The x-direction gas velocities and both components of the solids velocities were initially set to zero. The simulation was allowed to run for 0.4 s at a low inlet gas velocity. After that time, the inlet velocity was increased. This startup procedure reduces shock to the bed. Without this type of startup, the particulates would usually be blown out of the bed. The parameters used in the simulations for the three Geldart Groups are given in Table 1.

The bubble images were rendered with a demarcation in the void fraction at 0.8. The images were then read by the Image Magic Pro software (Image Pro, 1997). Bubbles that were open to the wall or the freeboard of the bed were not counted. Only bubbles that were fully enclosed were used in the count. The area of the bubble was calculated from the number of pixels that cover it. An equivalent diameter, d_{eq}, was then calculated from

$$d_{eq} = \sqrt{\frac{4a}{\pi}} \quad (36)$$

using the computed area, a, assuming the bubbles to be circular. In addition, the Sauder mean diameter, $d_{3,2}$, was calculated using

$$d_{3,2} = \frac{\Sigma d_{eq}^3}{\Sigma d_{eq}^2} \quad (37)$$

Table 2. Bubble Results for Geldart Group C, A and B Particles

Geldart Group	C	A	B
Number of bubbles	104	532	148
Sauder mean diameter (cm)	0.468	0.660	5.179
Average aspect ratio	1.94	2.59	20.52

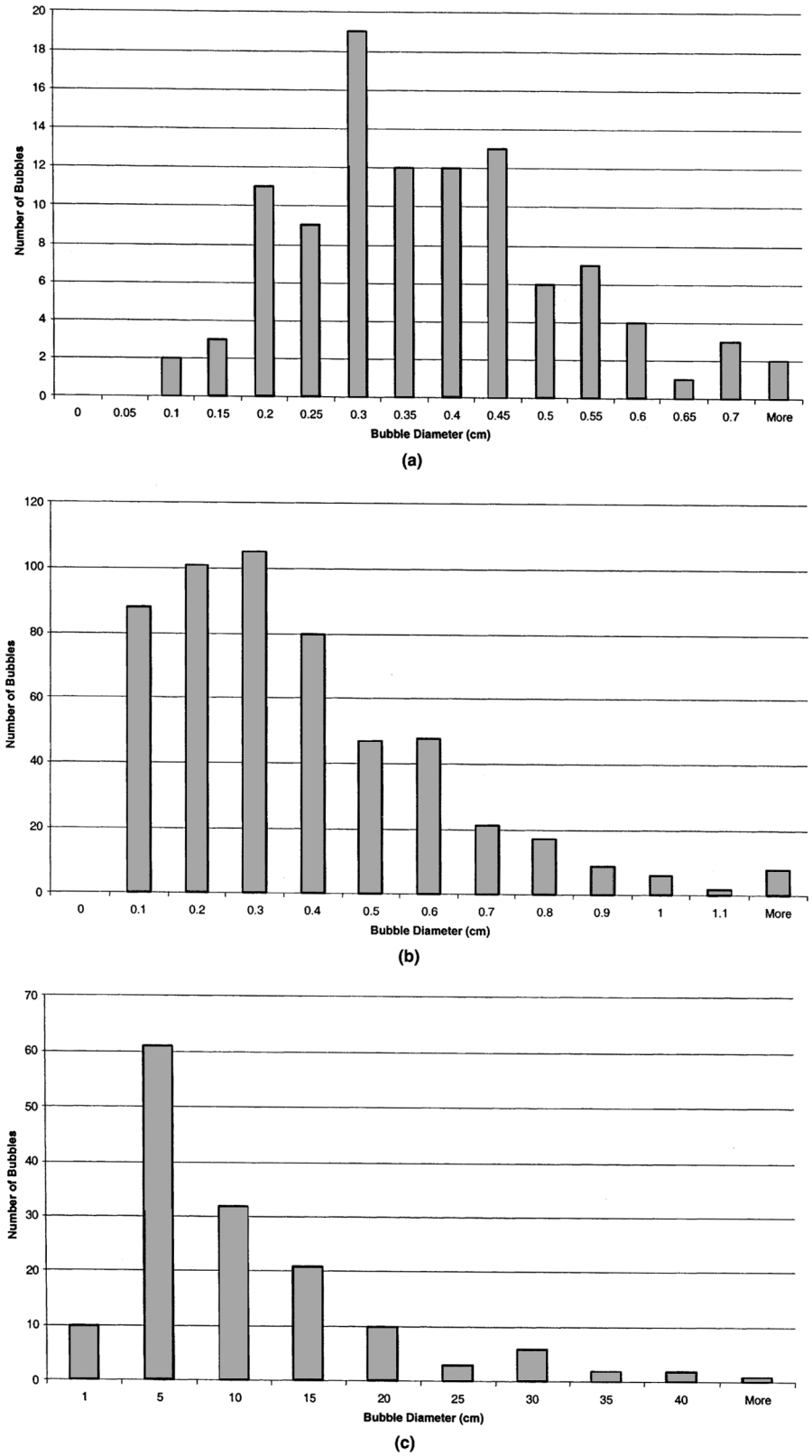

Figure 6. (a) Bubble-size distribution for Geldart Group C; (b) bubble-size distribution for Geldart Group A; (c) bubble-size distribution for Geldart Group B.

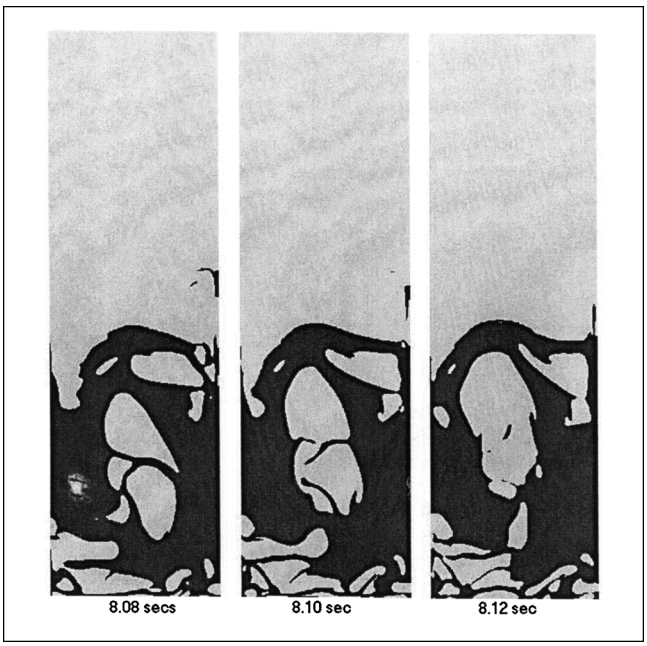

Figure 7. Coalescences of computed bubbles for Geldart Group B particles.

The bubbles computed for Geldart Group A and Group C are similar in diameter, although Group A's Sauder mean diameter was slightly larger than Group C. However, the number of bubbles in the Geldart Group A simulations is substantially more than in the Geldart Group C simulation. This may simply be due to the larger volume of gas being added to the bed. The bed consisting of Geldart Group C particles had a larger bed expansion compared to Geldart Group A because there were no cohesive forces used in the simulation.

Typical snapshots of the computed bubbles are shown in Figure 5. A bubble-size analysis was completed for each Geldart Group. The bubble diameters were measured from 11 images taken from each simulation. The images of void fraction were taken at 0.5-s intervals between 5 and 10 s of the simulations.

A summary of bubble statistics is shown in Table 2. The full histograms of bubble diameter are included in Figure 6. The histograms indicate marked differences between the mean bubble diameters and their distribution about the mean. Corresponding histograms were computed for the bubble aspect ratio, defined to be the ratios of bubble heights to widths, and were also found to clearly distinguish between the Geldart Groups.

Davidson and Harrison (1963) proposed a theory for the estimate of the maximum stable bubble size. The maximum bubble size is obtained by equating the terminal velocity to the bubble rise velocity to obtain

$$(d_e)_{\max} = 2.0\frac{(v_T^*)^2}{g} \tag{38}$$

Grace (1982) has reviewed Davidson and Harrison's theory. For the Geldart Group A case investigated here, Eq. 38 predicts that the maximum bubble diameter would be 0.906 cm. This value is consistent with the average bubble diameter of 0.660 cm obtained in the simulation. Although the theory was developed for Geldart Group A particles, it predicts a maximum bubble diameter of 30 cm, in surprising agreement with an average bubble diameter of 20.5 cm for the simulation of Geldart Group B particles.

Kunii and Levenspiel (1991) also make predictions of bubble diameters for Geldart Groups A and B. Their work considers the ratio of inlet velocity to minimum fluidization ve-

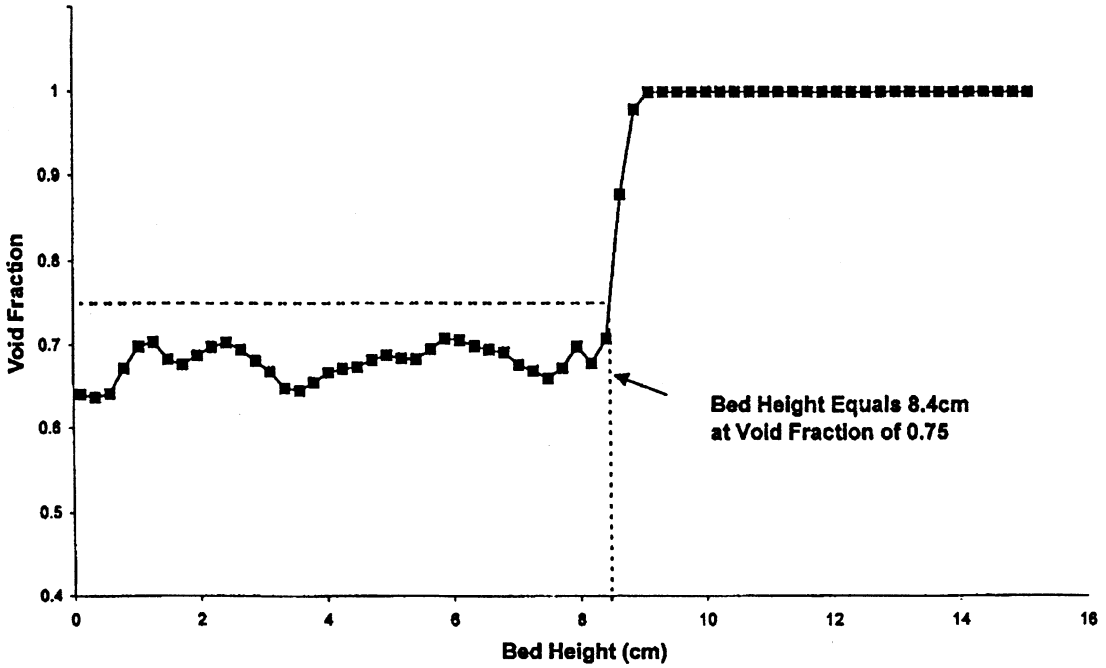

Figure 8. Typical void-fraction profile for the bubbling bed at a given time for Geldart Group A.

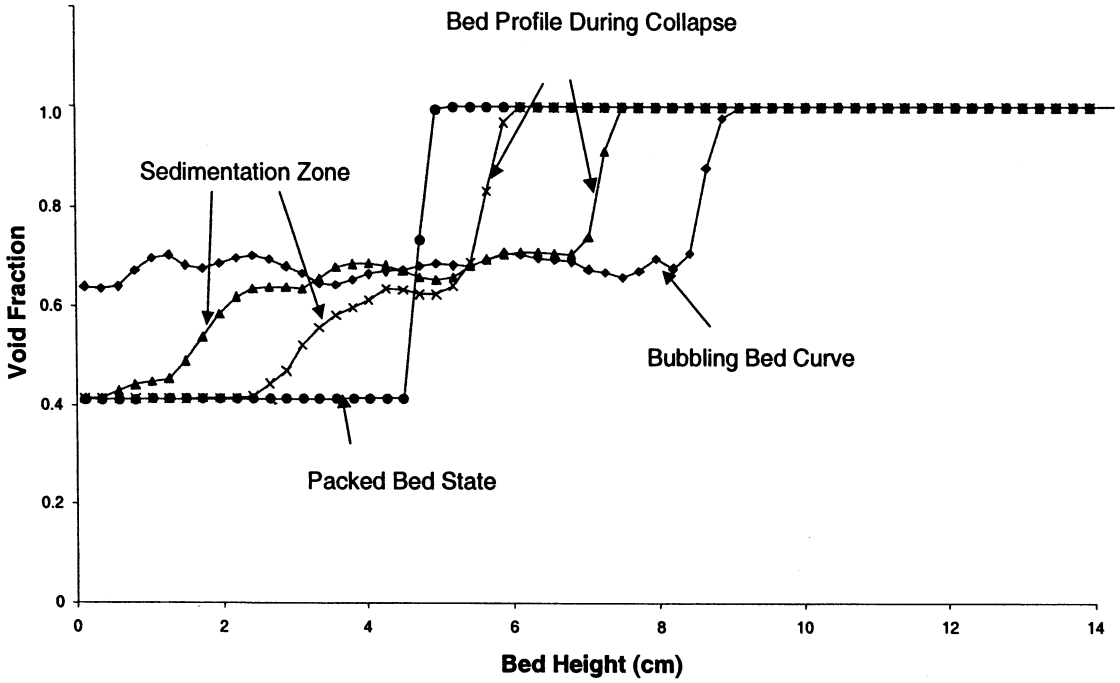

Figure 9. Example of void-fraction profiles for Syamlal et al. (1993) solids modulus during bed collapse for Geldart Group A particles.

locity, as well as the distance above the distributor. For the Geldart Group A simulations, the predicted equivalent bubble diameter 5 cm above the distributor ranges between 0.2 to 4.0 cm. The simulated bubble diameter of 0.66 cm lies in this range.

For the Geldart Group B simulation, the ratio of inlet gas (superficial) velocity to minimum fluidization velocity (35 cm/s)/(3.2 cm/s), was very close to that of the Geldart Group A simulations (3.0 cm/s)/(0.32 cm/s), even though the absolute numbers are an order of magnitude larger. Based on the Kunii and Levenspiel (1991) equivalent bubble-diameter correlations, this would give the same predicted bubble diameter for both Geldart Groups A and B. The computer simulation gave significantly different bubble diameters for Groups A

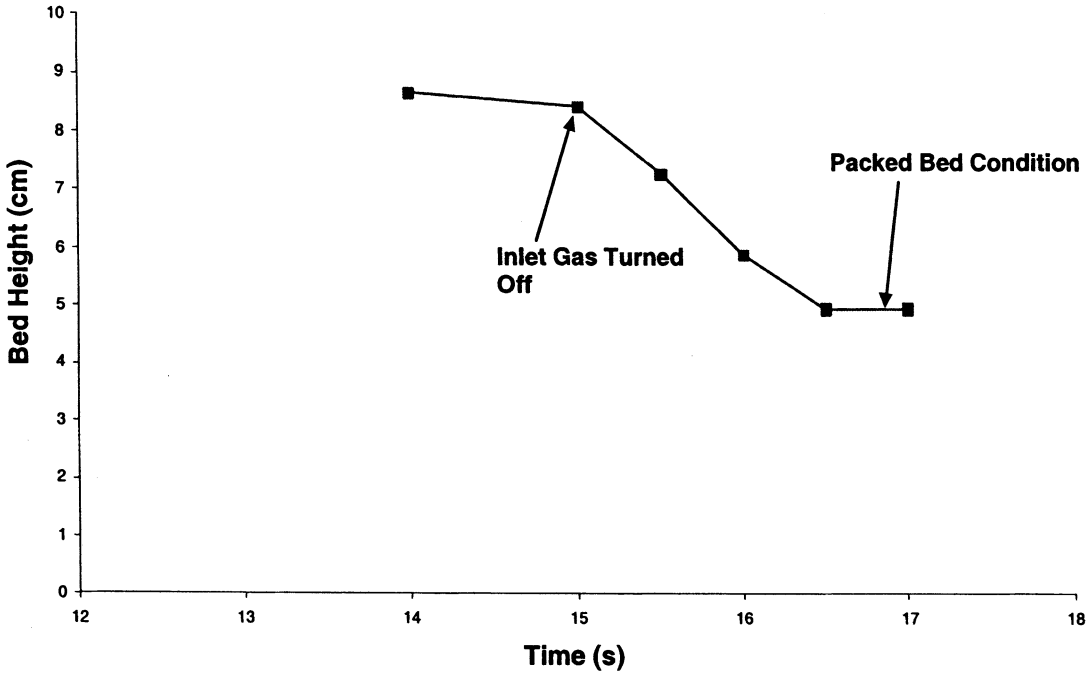

Figure 10. Typical bed collapse curve for Geldart Group A particles.

and B. Yang et al. (1983) determined that for Geldart Group B particles, bubbles could be very large. For very high flow rates, bubbles are predicted to be up to 1 m in diameter. The simulation for Group B particles gave a predicted bubble diameter of 5.179 cm, about one-third of the bed width of 15 cm.

The Geldart Group B simulation produced large bubbles that split and coalesced regularly, as shown in Figure 7. The simulations did an excellent job at demonstrating the different behavior of the fluidized bed for different particles sizes.

Turbulence of Geldart Group A Particles

Turbulence characteristics of Geldart Group A fluidization were computed using standard relationships involving variances and covariances of particle velocities. For the Geldart Group A parameters given in Table 1, it was found that there was generally upflow in the center of the bed and downflow near the walls. A video of the simulation and velocity vector plots reported in Gelderbloom (2001) shows transient vortices that give rise to very high turbulence typical of Geldart Group A particles (Cody et al., 1996). The Reynolds stresses $\langle V'V' \rangle$ and $\langle U'U' \rangle$, were computed to be approximately equal to 40 $(\text{cm/s})^2$. Therefore the granular temperature, Θ, is also 40 $(\text{cm/s})^2$. The turbulent intensity defined as the square root of the granular temperature divided by the inlet (superficial) gas velocity, 3 cm/s, given in Table 1, gives a value of 2.1, which is remarkably high. However, Cody et al. (1996) have experimentally determined turbulent intensities that are even higher than this computed value for lower superficial gas velocities. The computed value of the turbulent intensity agrees with these data.

The computed Reynolds stress, $\langle U'V' \rangle$, was found to be an order of magnitude smaller than the granular temperature, as expected. A grid independence study is presented in Gelderbloom (2001). For a grid size of 60×130, fewer bubbles are formed than for the case of 90×195 shown in Table 1. As the grid size is decreased further (30×65), very few bubbles are formed. For a grid size of 12×25, no bubbles are formed. For all these cases, the time-averaged bed expansion decreases from the base case in Table 1.

Simulation of the Collapsing Fluidized Bed

The same simulations for the bubbling fluidized bed as described in the "Computed Bubbles for Geldart Groups C, A, and B" section and listed in Table 1, were used for the collapsing fluidized-bed simulations.

Each simulation was run for 10 to 25 s until a quasi-steady-state condition was reached. At that time the inlet gas flow was shut off initiating the bed collapse. The simulation was continued until the bed completely collapsed into a consolidated state.

A typical void fraction plot for the bubbling bed at a given time is shown in Figure 8 for a Geldart Group A simulation. This plot is generated by computing the average void fraction across the width of the bed at each vertical grid. These average void fractions were then used to determine the bed height, sedimentation zone, and the degree of consolidation. The void fraction in the 0- to roughly 8-cm bed height shown in Figure 8, defines the dense or emulsion region of the bed. The variation is due to bubbles present in the bed. The bed height or

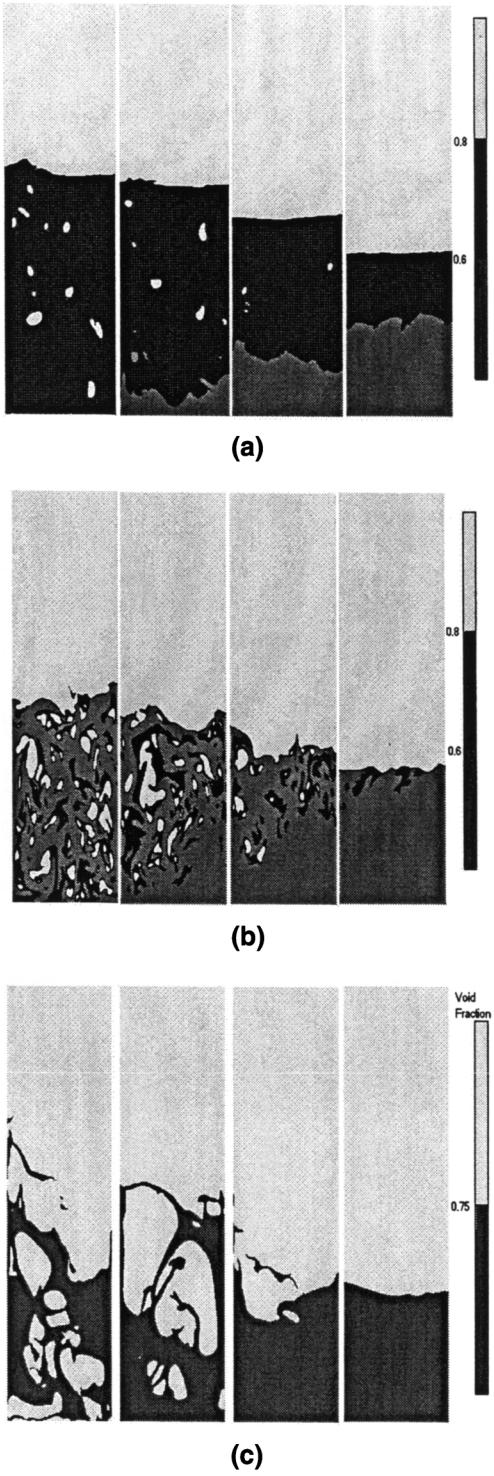

Figure 11. (a) Time sequence of void-fraction contours of a collapsing bed of Geldart Group C particles; (b) time sequence of void-fraction contours of a collapsing bed of Geldart Group A particles; (c) time sequence of void-fraction contours of a collapsing bed of Geldart Group B particles.

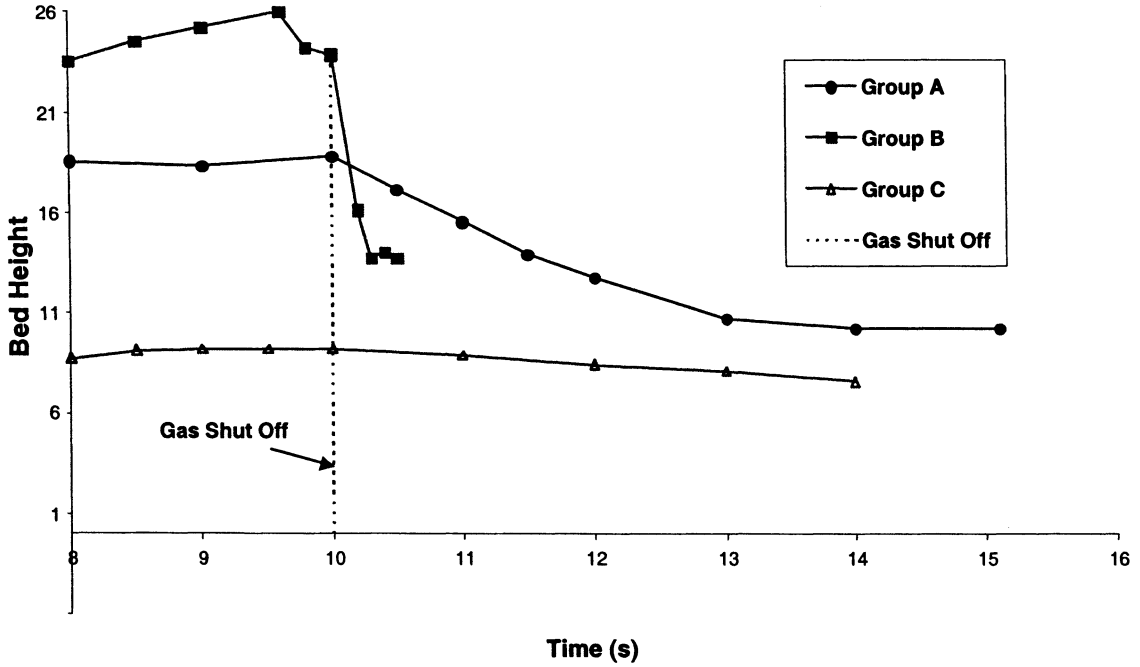

Figure 12. Collapse curves for Geldart Group C, A, and B particles.

freeboard is usually easily determined, as shown here. At other times the shape of the curve near the bed height is less sharp. For quantitative analysis, a void-fraction value of 0.75 was used to determine the location of the bed height, which in Figure 8 is 8.4 cm.

Once the gas is turned off, the bed begins to collapse, as shown in Figure 9. Each curve, other than the bubbling-bed curve, is at a later time. It is clear that the bed height eventually collapses to approximately 4.8 cm and the consolidation portion of the bed has reached its maximum height. In this example, the bed achieves a consolidated state having a void faction of 0.42 and a height of approximately 4.8 cm, and the bed dynamics stop when the entire bed reaches the packed bed state.

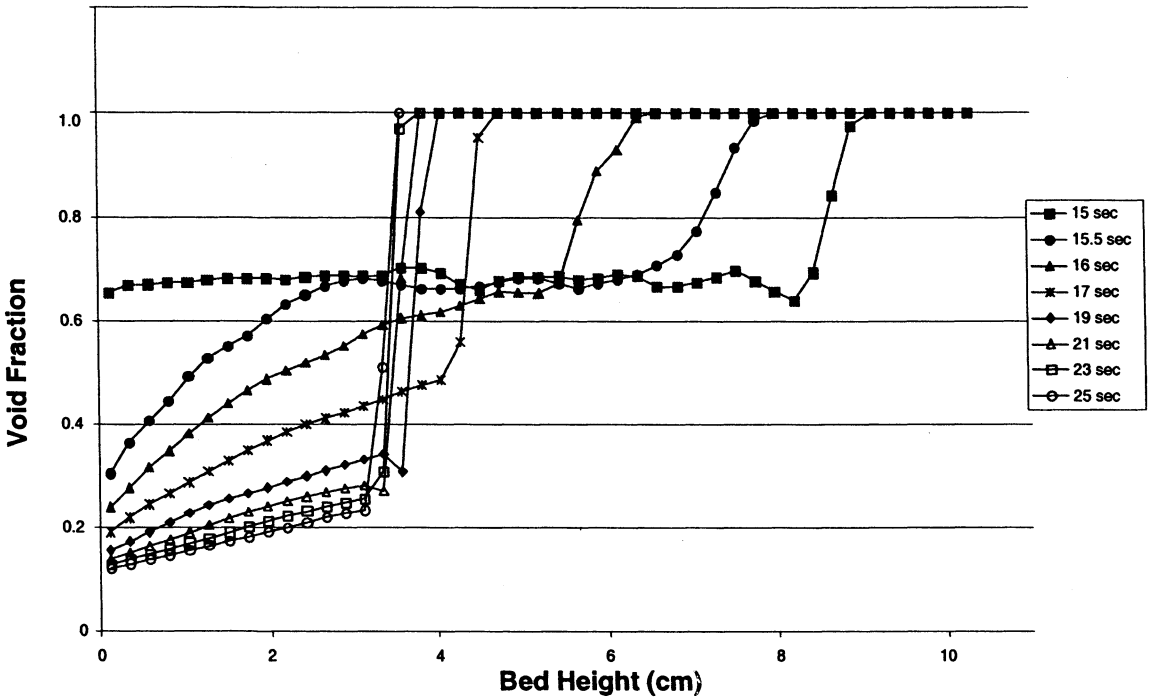

Figure 13. Void-fraction change during bed collapse for Gidaspow and Ettehadieh (1983) solids modulus for Geldart Group A.

From the void fraction vs. bed-height plots, the bed height vs. time plot is generated. As was already mentioned, the void-fraction value of 0.75 is used to determine the bed height. The bed height vs. time plot for the example shown in Figure 9 is plotted in Figure 10. The collapse velocity is then calculated from the bed height vs. time data from the initiation of the gas being shut off at 15 s to the initial achievement of the packed-bed state at 16.5 s, approximately 2.4 cm/s. The shape of the curve is not always as linear and sometimes has an irregular start to the collapse portion of the curve. This is due to the presence of a bubble near the bed height just as the gas is shut off.

Void-fraction plots of the three Geldart Groups are shown in Figures 11a, 11b, and 11c. Comparison of the three bed-collapse sequences confirms the assertion set forth in the "Variability of Experimental Results" section that the bubble escape and sedimentation stages occur simultaneously. Bubbles are present in the dense phase of the bed almost to the time that the consolidation stage begins.

Significant differences in the collapse curves were observed, as shown in Figure 12. These curves were generated using the MFIX (Syamlal et al., 1993) solids modulus, G. The results do not differ significantly from those computed using the Bouillard et al. (1989) solids modulus. However, the consolidation region is significantly different for the Ettehaieh and Gidaspow (1983) solids modulus, as shown in Figure 13 for Geldart Group A particles. The collapse time for the bed containing Geldart Group C particles, as shown in Figure 12, is significantly longer than that of Geldart Groups A or B.

As disucssed by Yang et al. (1997) the faster collapse of fluidized beds containing Geldart Group C particles is due to the strong tendency for aggregation. This particle–particle attraction causes cracks or channels to form, allowing the gas to escape quickly. This phenomenon is not modeled in the simulation.

For Geldart Groups A and B simulations, the collapse curve shapes are in agreement with what has been discussed in the literature. In addition to matching the correct shape of the collapse curve, the collapse velocity values during the bubble escape/sedimentation stage closely match Barreto et al.'s (1988) theory, which suggests that the inlet fluidizing-gas velocity rate is equal the bed-height collapse rate.

Barreto et al.'s theory is a nonhydrodynamic model consisting of bubbling, emulsion, and wake phases. The finding that the collapse velocity is equal to the superficial velocity before the bed collapse is a significant test of the predictive capability of the hydrodynamic model, which does not explicitly assume the existence of such phases. It is amazing to find that the collapse velocity is exactly equal to the superficial gas velocity for collapsing beds consisting of nanoparticles as well (Jung and Gidaspow, 2003; Wang et al., 2001).

When the computed collapse velocities for Geldart Groups C, A, and B are plotted as a function of inlet (superficial) gas velocity, they agree with the predictions of Barreto et al.'s (1988) theory, as shown in Figure 14. The computed collapse rate for Geldart Group B agrees with the data of Yang et al. (1997), who present no theory.

Effect of Viscosity and Drag on the Collapse of a Bubbling Fluidized Bed

The simulation using two expressions for the solids viscosity, $\mu_s = 5\epsilon_s$ poise ($0.5\epsilon_s$ Pa·s) and $\mu_s = 60\epsilon_s$ poise ($6.0\epsilon_s$ Pa·s) for the case of Geldart Group A particles, were performed. The expression completely overrides the models given

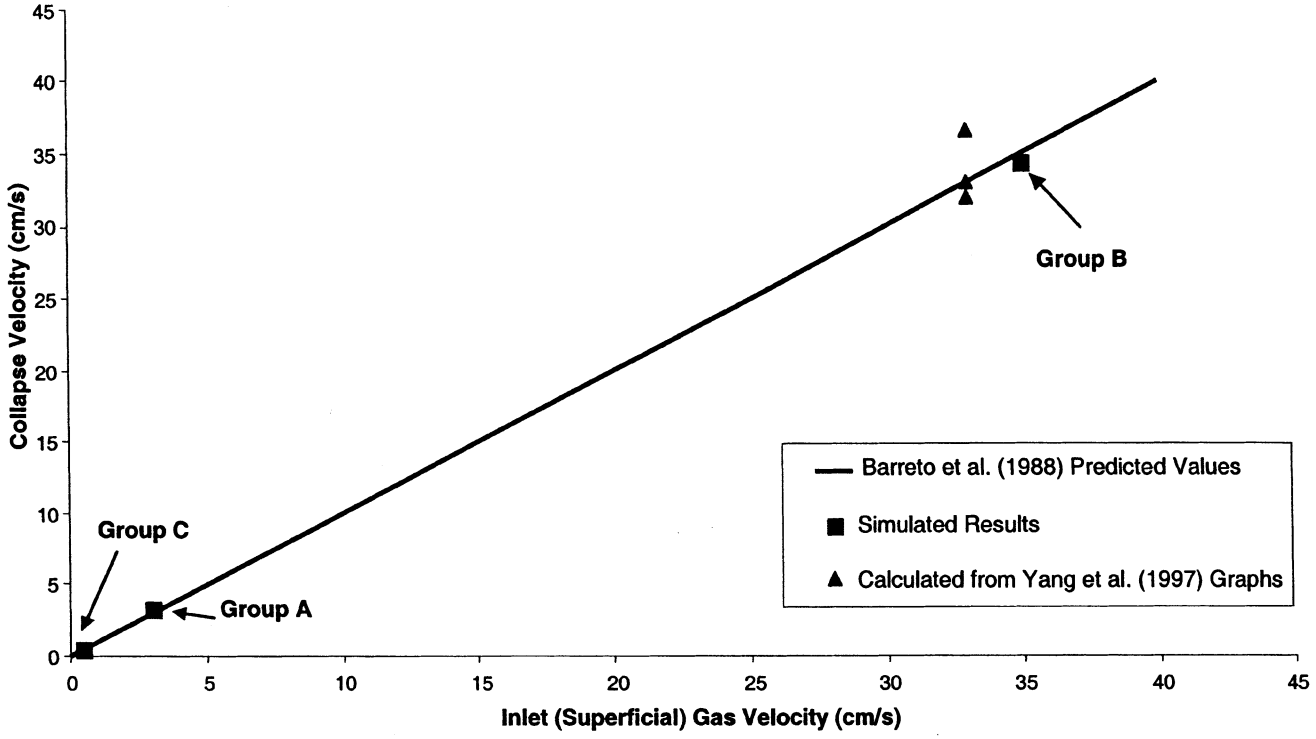

Figure 14. Experimental and simulation results vs. predicted collapse velocity.

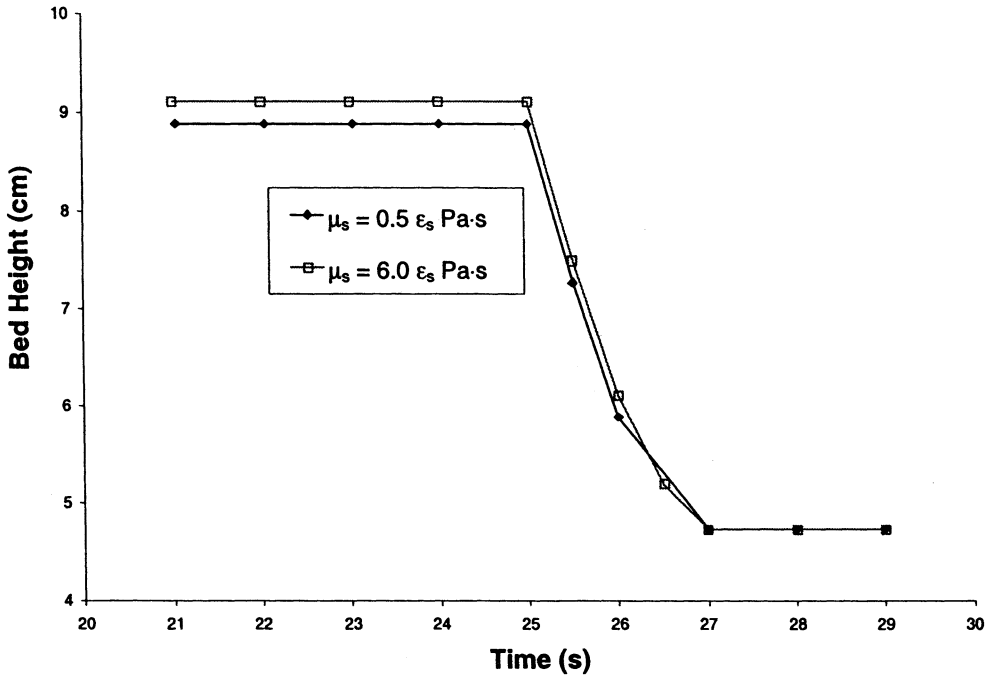

Figure 15. Bed collapse for different solids viscosity functions.

in the MFIX code (Syamlal et al., 1993). The collapse curves are shown in Figure 15. The bed expansion was slightly higher for the higher viscosity material model, which may be due to increased entrapment of air in the bed. Upon collapse, the two beds behaved very similarly, collapsing to a packed-bed state in the same amount of time. From this evidence it can be concluded that collapse time of the bed is not a function of the solids viscosity.

The simulations were compared using two different drag functions for the bubbling and collapsing fluidized bed containing Geldart Group A particles. The MFIX (Syamlal et al., 1993) and modified Ergun (Gidaspow, 1994) drag models were investigated. Results in Figure 16 show a slight difference in the expanded bed heights of the bed. At the time the gas is turned off at 10 s, there is a 0.69 cm difference in bed height. This height difference is exaggerated by the presence

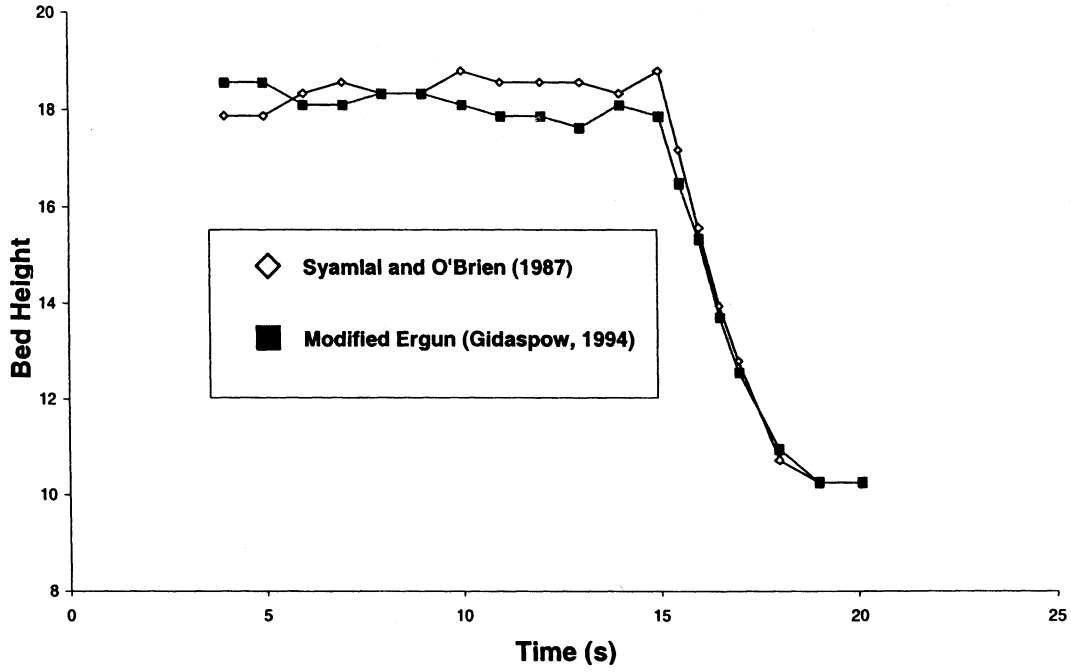

Figure 16. Bed collapse with different drag functions.

and release of bubbles. The collapse curves have the same shape and the same amount of time elapses before reaching the packed-bed state. It is concluded that the difference between these two drag functions is not significant and any reasonable function for drag does not affect the collapsing of the bed. Van Wachem et al. (2001) reached a similar conclusion.

Conclusions

1. This article shows that numeric simulations can distinguish between the three Geldart Groups C, A, and B for both the bubble sizes and collapse rates.

2. The computed turbulent intensity for Geldart Group A particles is higher than unity, in agreement with the granular temperature measurements of Cody et al. (1996).

3. The computed bubble sizes are in agreement with the classic expression for the maximum stable bubble size. The code also computes the complete distribution of the bubble size for the three Geldart Groups. The classic expression does not account for such a distribution. In these simulations, a restitution coefficient of 0.8 was assumed. There is a need to determine this parameter experimentally by performing more granular temperature measurements and to determine its effect on bubble sizes and distributions.

4. The CFD code models produce the collapse velocity, in agreement with experimental data, as shown in Figure 14.

5. The consolidation phase for the collapsing bed experiment is a strong function of the solids modulus, G. Therefore, we suggest that such a function be determined experimentally for the Geldart Groups. In a follow-up study Jung and Gidaspow (2002) determined this modulus for 10-nm-dia. fumed silica particles and a computer modeled the bed-collapsing process using the theory presented in this article. Since the nanosize particles form clusters, an empirical cluster diameter was used in the simulation in place of the actual diameter, as used here.

6. The bubble escape–sedimentation zone collapse rate, which was found to occur simultaneously, is not a strong function of various drag models or solids rheology.

Acknowledgments

We thank the Dow Corning Corporation for their support for this work, and M. Syamlal of Fluent, Inc., for his technical support with the MFIX computer code.

Notation

C_{flm} = coefficient of friction between solids phases l and m
d_p = particle diameter
$d_{p\lambda}$ = particle diameter of solids phase λ, m
$(d_e)_{\max}$ = maximum diameter of bubble, cm
d_{eq} = equivalent diameter of circle, cm
$d_{2,3}$ = Sauder mean diameter, cm
$\overline{\overline{D}}_g$ = rate of strain tensor, fluid phase, Eq. 6, s^{-1}
$\overline{\overline{D}}_s$ = rate of strain tensor, solids phase, Eq. 11, s^{-1}
e_m = coefficient of restitution for mth solids phase
e_{lm} = coefficient of restitution for the collisions of mth and lth solid phases
F_{gs} = coefficient for the interphase force between the fluid phase and the solids phase, $= F_{sg}$ kg/(m^3·s)
F_{slm} = coefficient for the interphase force between the lth solids phase and the mth solids phase, kg/(m^3·s)
$\boldsymbol{g}$ = acceleration due to gravity, m/s^2
$g_{o_{lm}}$ = radial distribution function at contact
G = solids elasticity modulus, Pa
P_g = pressure in the fluid phase, Pa
P_s = pressure of solids phase, Pa
P_s^p = pressure in solids phase, plastic regime, Pa
P_s^v = pressure in solids phase, viscous regime, Pa
P^* = total solids pressure in plastic regime, Pa
t = time, s
u = horizontal velocity, x-direction, m/s
U' = fluctuating velocity, x-direction, m/s
$\boldsymbol{v}_g$ = fluid phase velocity vector, m/s
$\boldsymbol{v}_s$ = solids phase velocity vector, m/s
ν_{sl}, ν_{sm} = velocity vectors for the lth and the mth solids phases, m/s
v_t^* = terminal settling velocity, m/s
v = vertical velocity, y-direction, m/s
V' = fluctuating velocity, y-direction, m/s

Greek letters

ϵ_g = volume fraction of the fluid phase (void fraction)
ϵ_s = volume fraction of the solids phase
$\epsilon_{s\lambda}$ = volume fraction of solids phase $s\lambda$
Θ = granular temperature of solids phase, m^2/s^2
λ_s^v = second coefficient of solids viscosity, viscous regime, kg/(m·s)
μ_g = molecular viscosity of the fluid phase, kg/(m·s)
μ_s^p = solids viscosity, plastic regime, kg/(m·s)
μ_s^v = solids viscosity, viscous regime, kg/(m·s)
ρ_g = microscopic (material) density of the fluid phase, kg/m^3
ρ_s = microscopic (material) density of the solids phase, kg/m^3
$\overline{\overline{\tau}}_g$ = fluid-phase stress tensor, Pa
$\overline{\overline{\tau}}_s$ = solids-phase stress tensor, Pa
$\overline{\overline{\tau}}_s^p$ = solids-phase granular stress tensor, plastic regime, Pa
$\overline{\overline{\tau}}_s^v$ = solids-phase granular stress tensor, viscous regime, Pa
Φ = angle of internal friction

Literature Cited

Abrahamsen, A. R., and D. Geldart, "Behavior of Gas-Fluidized Beds of Fine Powders Part II. Voidage of the Dense Phase in Bubbling Beds," *Powder Technol.*, **26**, 47 (1980).

Barreto, G. F., G. D. Mazza, and J. G. Yates, "The Significance of Bed Collapse Experiments in the Characterization of Fluidized Beds of Fine Powders," *Chem. Eng. Sci.,* **43**(11), 3037 (1988).

Bouillard, J. X., D. Gidaspow, and R. W. Lyczkowski, "Porosity Distributions in a Fluidized Bed With an Immersed Obstacle," *AIChE J.,* **35**(6), 908 (1989),

Bouillard, J. X., and D. Gidaspow, "On the Origin of Bubbles and Geldart's Classification," *Powder Technol.*, **68**, 13 (1991).

Cody, G. D., D. J. Goldfarb, G. V. Storch, Jr., and A. N. Norris, "Particle Granular Temperature in Gas Fluidized Beds," *Powder Technol.*, **87**, 211 (1996).

Davidson, J. F., and D. Harrison, *Fluidised Particles*, Cambridge Univ. Press, London (1963).

Enwald, H., E. Peirano, and A. E. Almstedt, "Eulerian Two-phase Flow Theory Applied to Fluidization," *Int. J. Multiphase Flow*, **22**(Suppl.), 21 (1996).

Formisani, B., R. Girimonte, and G. Pataro, "The Influence of Operating Temperature on the Dense Phase Properties of Bubbling Fluidized Beds of Solids," *Powder Technol.*, **125**, 28 (2002).

Garside, J., and M. R. Al-Dibouni, "Velocity-Voidage Relationships for Fluidization and Sedimentation," *Ind. Eng. Chem. Proc. Des. Dev.*, **16**, 206 (1977).

Geldart, D., "Types of Gas Fluidisation," *Powder Technol.*, **7**, 285 (1973).

Geldart, D., N. Harnby, and A. C. Y. Wong, "Fluidization of Cohesive Powders," *Powder Technol.*, **37**, 25 (1984).

Geldart, D., and A. C. Y. Wong, "Fluidization of Powders Showing Degrees of Cohesiveness—II. Experiments on Rates of De-Aeration," *Chem. Eng. Sci.*, **40**(4), 653 (1984).

Gelderbloom, S. J., "Computational Fluid Dynamic Simulation for Bubbling and Collapsing Fluidized Beds," PhD thesis, Illinois Institute of Technology, Chicago (2001).

Gidaspow, D., *Multiphase Flow and Fluidization Continuum and Kinetic Theory Descriptions*, Academic Press, San Diego (1994).

Gidaspow, D., and B. Ettehadieh, "Fluidization in Two-Dimensional Beds with a Jet; 2. Hydrodynamic Modeling," *Ind. Eng. Chem. Fundam.*, **22**, 193 (1983).
Gidaspow, D., and L. Huilin, "Equation of State and Radial Distribution Function of FCC Particles in a CFB," *AIChE J.*, **44**(2), 279 (1998).
Grace, J. R., "Fluidized Bed Hydrodynamics," *Handbook of Multiphase Systems*, Chap. 8, G. Hetsroni, ed., McGraw-Hill, New York, p. 8.20 (1982).
Grace, J. R., "Agricola Aground: Charaacterization and Interpretation of Fluidization Phenomena," *Fluidized Processes: Theory and Practice*, AIChE Symposium Series No. 289, Vol. 88, A. J. Weimer, ed., American Institute of Chemical Engineers, New York, p. 1 (1992).
Image-Pro Plus[tm], Media Cybernetics Version 3.0.1; 8484 Georgia Avenue, Silver Spring, MD 20910, USA; http://www.mediacy.com (1997),
Jackson, R., *The Dynamics of Fluidized Particles*, Cambridge Univ. Press, New York (2000).
Johnson, P. C., and R. Jackson, "Frictional-Collisional Constitutive Relationships for Granular Materials with Application to Plane Shearing," *J. Fluid Mech.*, **176**, 67 (1987).
Jung, J., and D. Gidaspow "Fluidization of Nano-Size Particles," *J. Nanopart. Res.,* in press (2003).
Kuipers, J. A. M., B. P. B. Hoomans, and W. P. M. Swaaij, "Hydrodynamic Models of Gas Fluidized Beds and Their Role for Design and Operation of Fluidized Bed Chemical Reactors," *FLUIDIZATION IX, Proc. Engineering Foundation Conf. on Fluidization*, L.-S. Fan and T. M. Knowlton, eds., Engineering Foundation, New York, p. 15 (1998).
Kunii, D., and O. Levenspiel, *Fluidization Engineering*, 2nd ed., Buttworth-Heinemann, Stoneham, MA (1991).
Lebowitz, J. L. "Exact Solution of Generalized Percus-Yevick Equation for a Mixture of Hard Spheres," *Phys. Rev.*, **A133**, 895 (1964).
Lettieri, P., "Study of the Influence of Temperature on the Flow Behavior of Solid Materials in a Gas Fluidized Bed," PhD Thesis, Univ. College London, London, UK (1999).
Lun, C. K. K., S. B. Savage, D. J. Jeffrey, and N. Chepurniy, "Kinetic Theories for Granular Flow: Inelastic Particles in Couette Flow and Slightly Inelastic Particles in a General Flow Field," *J. Fluid Mech.*, **140**, 223 (1984).
Rietema, K., "Application of Mechanical Stress Theory to Fluidization," *Proc. Int. Symp. On Fluidization*, A. A. H. Drinkenburg, ed., Netherlands Univ. Press, Eindhoven, The Netherlands, p. 154 (1967).
Rietema, K., "The Dynamics of Fine Powders, "Elsevier Science Publishing Co., Inc., New York, 57 (1991).
Syamlal, M., "A Review of Granular Stress Constitutive Relations," Topical Rep., U.S. Department of Energy, Office of Fossil Energy, Morgantown Energy Technology Center, Morgantown, WV, National Technical Information Service, Springfield, VA (1987).
Syamlal, M., and T. J. O'Brien, "A Generalized Drag Correlation for Multiparticle Systems," Unpublished report U.S. Department of Energy, Office of Fossil Energy, Morgantown Energy Technology Center, Morgantown, WV (1987).
Syamlal, M., Fluent, Inc. Personal communication, spread sheet sent directly to first author for drag correlations (1999).
Syamlal, M., W. Rogers, and T. J. O'Brien, "MFIX Documentation Theory Guide," Tech. Note, U.S. Department of Energy, Office of Fossil Energy, Morgantown Energy Technology Center, Morgantown, WV, National Technical Information Service, Springfield, VA (1993).
Tianxiong, L., C. Duo, W. Yousheng, and P. Chengzhong, "Characteristics of Fine-Powder Fluidized Bed," *Fluidization: Science and Technology: Conference Papers, China-Japan Symposium*, Science Press, Beijing, p. 57 (1982).
Tung, Y., and M. Kwauk, "Dynamics of Collapsing Fluidized Beds," *Fluidization: Science and Technology: Conference Papers, China-Japan Symposium*, Science Press, Beijing, p. 155 (1982).
Van Wachem, B. M. G., J. C. Schouten, C. M. van den Bleek, R. Krishna, and J. L. Sinclair, "Comparative Analysis of CFD Models of Dense Gas-Solid Systems," *AIChE J.*, **47**, 1035 (2001).
Weimer, A. W., and G. J. Quarderer, "Effect of Temperature on the Dense Phase in High Pressure Fluidized Beds of Fine Powders," *Fluidization and Fluid Particle Systems, AIChE Symp. Ser.*, No. 241 Vol. 80, American Institute of Chemical Engineers, New York, p. 79 (1984).
Yang, G., F. Wei, Y. Jin, Z. Yu, and Y. Wang,"Unique Properties of 30-μm Particles as the Catalyst of Fluidized-Bed Reactors," *AIChE J.*, **43**(5), 1190 (1997).
Yang, W.-C., D. Revay, R. G. Anderson, E. J. Chelen, D. L. Keairns, and D. C. Ceicro, "Fluidization Phenomena in a Large Scale Cold Flow Model," *Fluidization Engineering Foundation Conf. Proc., Int. Conf. on Fluidization*, United Engineering Foundation, New York, p. 77 (1983).
Wang, Y., F. Wei, Y. Jin, and T. Luo, "Bed Collapse Behavior of Primary Nanoparticles," *Fluidization X, Proc. Engineering Foundation Conf. on Fluidization*, Engineering Foundation, New York, p. 477 (2001).

Manuscript received Feb. 25, 2002, and revision received Sept. 30, 2002.